Chapter 11
Attosecond Molecular Spectroscopies with XUV Harmonic Radiation

R. Guichard, J. Caillat, S. Haessler, Z. Diveki, T. Ruchon, P. Salières, R. Taïeb, and A. Maquet

Abstract When irradiated by an intense pulse of an infrared (IR) laser, molecules emit a coherent radiation composed of a frequency comb of harmonics of the pump laser frequency, ranging from ultraviolet (UV) up to soft X-rays. These harmonics are emitted during extremely short time windows, within the attosecond range. The properties of harmonic emission are of much interest when applied to issues of relevance to AMOP (Atomic, Molecular and Optical Physics) and they have opened a new domain of investigation in the emerging field of attophysics. In the spectral domain, analyzing high harmonic spectra provides original information on the electronic structure of the outer orbitals that are active in the generation process. In the time domain, the use of attosecond pulses of Extreme Ultra-Violet (XUV) harmonics within a pump-probe scheme opens unique opportunities to develop a new time-resolved spectroscopy of transient excited molecular states. In this review, we shall report on recent advances in the field and we shall address several issues of interest with the objective to go beyond the "proof-of-principle" demonstrations that have been reported so far.

11.1 Introduction

Uncovering time-dependent aspects of chemical reactivity with unprecedented time resolution, in the attosecond range, has become achievable through the recent advent of harmonic-based sources of XUV radiation. In this context, two distinct kinds of applications of these new sources have been explored so far. In a chronological

R. Guichard · J. Caillat · R. Taïeb · A. Maquet (✉)
Laboratoire de Chimie Physique-Matière et Rayonnement (LCPMR), UPMC Université Paris 6, UMR 7614, 11 rue Pierre et Marie Curie, 75231 Paris Cedex 05, France
e-mail: alfred.maquet@upmc.fr

Z. Diveki · T. Ruchon · P. Salières
Service des Photons, Atomes et Molécules, CEA-Saclay, IRAMIS, 91191 Gif-sur-Yvette, France

S. Haessler
Photonics Institute, Vienna University of Technology, Gusshausstrasse 27/387, 1040 Vienna, Austria

L. Plaja et al. (eds.), *Attosecond Physics*, Springer Series in Optical Sciences 177,
DOI 10.1007/978-3-642-37623-8_11,

order, the first one has been the detailed analysis of the harmonic spectra generated by aligned molecular systems. This provides valuable information about the electronic molecular states (dominantly the outer valence states) involved into the generation process. Moreover, the analysis of such time-resolved harmonic spectra is expected to provide new insights in the dynamics of the electronic processes at work when generated by a system in the course of a chemical change. The second one is the use of harmonics as a photoionization probe, to extend the XUV measurements performed with synchrotron sources. A typical example includes the study of the resonances embedded within the atomic or molecular continuum: synchrotron measurements display the spectral signatures of autoionizing states as well as of the so-called shape resonances. As we shall report, a most interesting feature of harmonic-based measurements is that they give direct access to the temporal characterization of these phenomena.

In the context of this class of attosecond-resolved measurements performed with coherent XUV radiation, it turns out that the intensities of the harmonic lines can be measured quite straightforwardly, while the harmonic phases are a priori less accessible. The precise determination of these latter provides the key to explore the time domain, as their energy derivative gives access to characteristic time delays, with attosecond time resolution, in the system under consideration. Several techniques have been implemented so far to measure the harmonic phases. Among them, we shall focus the presentation on a multicolor IR-XUV photoionization scheme dubbed RABBIT (Reconstruction of Attosecond Beating By Interference of Two-photon transitions) technique [1–3]. In the following, we will describe some of the recent advances that have been achieved with the help of this technique, both from the theory and experimental standpoints.

Focusing first on the characterization of High Harmonic Generation (HHG) spectra in aligned molecules, it is well established now that the phases and intensities of the spectral components are very sensitive probes of the molecular states involved in the generation process. The first milestone in this direction has been the "tomographic imaging" of a molecular *orbital*, derived from the analysis of the harmonic emission by aligned N_2 molecules with different orientations of the internuclear axis with respect to the polarization of the pump field. This procedure, based on the analysis of the scaled harmonic intensities with assumptions for the harmonic phases, has initially permitted to image the σ_g HOMO (Highest Occupied Molecular Orbital) which is dominantly involved in the generation process [4]. A more detailed characterization of such HHG emission, including the determination of the spectral phases, has revealed that the HHG process results in fact from a delicate combination of contributions originating from both the σ_g HOMO and from the nearest underlying orbital π_u HOMO-1 [5]. In specific laser conditions, i.e. when a particular laser intensity is chosen, disentangling the contributions of each orbital to the harmonic signal is made possible as the net result of all phase contributions is close to $\pi/2$, therefore encoding them in the real and imaginary parts of the harmonic dipole, respectively. However, when the pump laser intensity is varied, this distinction becomes unclear as the mixing of the two contributions appears to be spectrally and intensity dependent [6].

Still regarding HHG in aligned molecules, another important question has emerged about the possibility to *control* the attosecond emission by changing the molecular response. The basic idea relies on the dependence of the harmonic generation on the orientation of the molecular axis with respect to the polarization of the pump laser. For instance, in two-center systems, interference phenomena are expected to take place depending on the internuclear distance, the molecular alignment and the de Broglie wavelength of the recombining electron. It is expected that these parameters govern the harmonic intensities and phases, allowing a pulse shaping of the attosecond emission in given spectral regions. Interferences resulting from multi-orbital contributions could also allow such pulse shaping. This has been demonstrated in the test case of the linear CO_2 molecule [7].

A second (more recent) field of investigations deals with the molecular response to the attosecond pulses of harmonic XUV radiation generated in an auxiliary gas jet. Clearly, under such conditions, molecules can experience various excitation processes, including ionization and dissociation. However, given the unique temporal properties of harmonic pulses, the possibility arises to uncover the dynamics of excited "vibronic" molecular states. This implies to disentangle the electronic and nuclear degrees of freedom in reactive species. We shall show below that the RABBIT technique is again an efficient tool to achieve this goal [8, 9].

Central as an investigation tool in all the above listed topics is the RABBIT technique. It has been implemented in several experiments to realize the combined measurements of the phases and amplitudes of harmonic signals. For the sake of completeness, we shall devote Sect. 11.2 to a brief description of the technique. In Sect. 11.3, we shall discuss how molecular data can be extracted from the analysis of harmonic spectra generated in aligned molecules. Subsections will concentrate on multichannel (or multi-orbital) contributions and on the control of harmonic emission in the time domain. The main features of the recently developed attosecond XUV spectroscopy of molecular excited states will be outlined in Sect. 11.4, with applications to the relation between RABBIT phases and the timing of photoelectron emission in near-threshold transitions. The chapter will end in Sect. 11.5 with a brief discussion of the perspectives opened by these recent advances.

11.2 RABBIT Analysis of Harmonic Spectra

The RABBIT technique has been designed first with the objective to measure the relative phases of consecutive odd harmonics, as generated in a system with central symmetry. It is based on the multicolor ionization of an auxiliary atomic or molecular gas sample, in the simultaneous presence of an attenuated beam of the pump IR laser with frequency ω_L together with a comb of its odd XUV harmonics with frequencies $\Omega_\pm = (2q \pm 1)\omega_L$, [1–3]. In these conditions, the photoionization spectrum displays equidistant lines labelled $\ldots, H_{2q-1}, H_{2q+1}, \ldots$, that are associated to the absorption of single harmonic photons, and intermediate sidebands

$\ldots, \mathrm{SB}_{2q}, \ldots$ resulting from the exchange of one additional IR photon. In the moderate IR intensity regime considered, the sidebands result from two-photon IR-XUV ionization transitions.

Still in this regime, it turns out that two distinct quantum paths contribute dominantly to the formation of a given sideband SB_{2q}: (i) sequential absorption of H_{2q-1} and of the fundamental and (ii) sequential absorption of H_{2q+1}, followed by the stimulated emission of the fundamental. Two other quantum paths also participate which are associated to transitions with reversed time-ordering but, in the context considered here, their contributions are much smaller [1–3]. The dominant XUV-IR processes correspond to two-photon "Above-Threshold Ionization" (ATI) transitions. Then, RABBIT measurements consist in monitoring the variations of the sideband magnitude when the IR-XUV delay τ is varied. One shows that, as a result of the two quantum paths interferences', it can be written under the generic form below, which evidences that each sideband signal S_{2q} oscillates periodically as a function of τ:

$$S_{2q} = \alpha + \beta \cos(2\omega_L \tau + \Delta\phi_\Omega + \Delta\theta) \tag{11.1}$$

where α and β are real quantities, $\Delta\phi_\Omega = \phi_{2q+1} - \phi_{2q-1}$ is the difference between the intrinsic phases of the two consecutive harmonics and $\Delta\theta$ is a contribution that is characteristic of the ionized system. The latter term originates from the fact that the second-order transition amplitudes associated to ATI transitions are complex numbers, with phases that depend on the quantum path followed by the system to reach the sideband. Thus when clocked against the IR laser cycle, the periodic variations of the cosine term in the expression Eq. (11.1) contains both the phase informations about the harmonics as well as intrinsic molecular data contained in the $\Delta\theta$ term. If the continuum structure of the system under study is smooth, $\Delta\theta \approx 0$ and the measurement of the phases of the oscillations gives a direct access to the relative phases of the harmonics $\Delta\phi_\Omega$ and, by extension, to their emission time, with attosecond resolution [10, 11].

To make the connexion between phase differences and time delays clearer, it is convenient to rewrite the formula in Eq. (11.1) under the form:

$$S_{2q} = \alpha + \beta \cos\left[2\omega_L(\tau + \tau_{2q} + \tau_I)\right] \tag{11.2}$$

where $\tau_{2q} = (\phi_{2q+1} - \phi_{2q-1})/2\omega_L$ is a finite difference approximation to the group delay $GD = \partial\phi/\partial\omega$ of the harmonic radiation at the considered frequency, which is also called the "emission time", and $\tau_I = \Delta\theta/2\omega_L$ is an intrinsic time delay resulting from the analytical structure of the two-photon ATI transition amplitude in the system under consideration. For the sake of completeness we turn now to a succinct presentation of the origin of this additional phase or, equivalently, of this time delay.

The RABBIT technique is implemented with radiation fields with intensities moderate enough so that lowest-order time-dependent perturbation theory applies. Then, the structure of the relevant transition amplitudes dominantly involved in the process is the one of a second-order matrix element associated to a two-photon ATI transition . Each matrix element contains angular factors that may be complex quantities, but it turns out that they average out when performing the angular integration

of the squared amplitude that is required to reproduce the photoelectron signal. The phase difference $\Delta\theta$ in Eq. (11.1) originates from the radial parts of the amplitudes, which are complex numbers for ATI transitions.

This can be seen from their expression which is associated to the transition from an initial bound state with radial component $|R_{n_i,\ell_i}\rangle$ with negative energy ε_i towards a final state in the continuum $|R_{k_{2q},\ell_f}\rangle$ associated to photoelectrons in the sideband SB_{2q}, with kinetic energy: $\varepsilon_{2q} = k_{2q}^2/2 = \varepsilon_i + 2q\omega_L$. The transition results from the sequential absorption of one harmonic XUV photon $\Omega_\pm$ followed by the exchange of the IR photon ω_L. Thus, the radial component of the transition amplitude is of the following form:

$$T^{\pm}_{\ell_f,\ell,\ell_i}(\varepsilon_i + \Omega_\pm) = \sum_n \frac{\langle R_{k_{2q},\ell_f}|r|R_{n,\ell}\rangle\langle R_{n,\ell}|r|R_{n_i,\ell_i}\rangle}{\varepsilon_i + \Omega_\pm - \varepsilon_n} + \lim_{\epsilon\to 0^+}\int_0^{+\infty} d\varepsilon_k \frac{\langle R_{k_{2q}\ell_f}|r|R_{k,\ell}\rangle\langle R_{k,\ell}|r|R_{n_i,\ell_i}\rangle}{\varepsilon_i + \Omega_\pm - \varepsilon_k + i\epsilon}. \quad (11.3)$$

In this expression, we have made explicit the structure of the sum running over the whole atomic spectrum, by separating the contributions of the discrete states with negative energies $\varepsilon_n > \varepsilon_i$ and radial component $|R_{n,\ell}\rangle$ and of the states in the continuous spectrum, with energies ε_k and radial wave function $|R_{k,\ell}\rangle$. We note that the angular momentum algebra imposes the selection rules $\ell = \ell_i \pm 1$ and $\ell_f = \ell_i, \ell_i \pm 2$. Also, the radial wave functions are real quantities, so that, in the first term, the sum over the discrete spectrum is also real, with denominators which stay positive as $\Omega_\pm > |\varepsilon_i|$. By contrast, the second term, i.e. the integral over the continuous spectrum, is a complex number. This is because of the presence of a pole on the positive energy real axis located at $\varepsilon_k = \varepsilon_i + \Omega_\pm$. This implies that the integral acquires an imaginary component according to the prescription:

$$\lim_{\epsilon\to 0^+}\int_{-\infty}^{+\infty}\frac{dx}{x+i\epsilon} = \mathcal{P}\int_{-\infty}^{+\infty}\frac{dx}{x} - i\pi\delta(x) \quad (11.4)$$

where the Cauchy principal part in the first term is a real quantity while the second term with the delta function is pure imaginary. The consequence is that the amplitude attached to each quantum path leading to the sideband of interest acquires a phase, i.e.

$$T^{\pm}_{\ell_f,\ell,\ell_i}(\varepsilon_i + \Omega_\pm) = \left|T^{\pm}_{\ell_f,\ell,\ell_i}(\varepsilon_i + \Omega_\pm)\right| e^{i\theta_\pm}. \quad (11.5)$$

The quantity $\Delta\theta$ introduced in Eq. (11.1) is the difference $\Delta\theta = \theta_+ - \theta_-$ between the phases of the quantum path amplitudes leading to a given sideband. As we shall show below, this analytical structure of the RABBIT amplitudes play a most important role to address several phenomena of interest in attophysics that are investigated with the help of harmonics.

11.3 Harmonic Emission by Aligned Molecules

11.3.1 Multichannel Contributions to Harmonic Emission

Typical harmonic spectra generated in atoms exhibit the following general features: a rapid decay at the lowest orders, followed by a plateau where the harmonic intensity is roughly constant, and a final decay beyond the cutoff location. When generated in molecules, intensity minima and corresponding phase jumps appear in the emitted high-order harmonic signal. Three distinct classes of intensity minima, related either to structural or dynamical origins, have been evidenced. A representative type of "structural" minimum has been documented in two-center molecules [12, 13]. It appears when destructive interferences take place between XUV radiation emissions from each center. The harmonic frequency at which such minima are located depends on the molecular alignment with respect to the laser polarization θ, as well as on the internuclear distance R. It can be linked to the angular dependence of the recombination dipole moment of each contributing channel [7, 14, 15] and its position does not change with the laser parameters [12, 16]. Another type of minimum is referred to as "Cooper-like", since its presence can be related to the minima observed in the photoionization cross section of the species under study. They involve destructive interferences between either distinct angular momentum components of the unbound electron wave packet when it recombines with the initial state [17], or from the nodal structure of the initial state. The position of such minima is independent of any laser parameter—especially the intensity I_L, [18]. A third type of minima, referred to as "dynamical", occurs when several molecular orbitals (or channels) contribute to HHG. In the specific situations where two contributions end up with a π-phase difference and thus interfere destructively, a marked minimum appears in the harmonic spectrum. Varying the driving laser parameters—either intensity or wavelength—shifts their relative phase and thus modifies the spectral position of the dynamical minima [19, 20].

The discrimination between the different types of minima is therefore based on two main experimental parameters: θ and I_L. The presence of a so-called dynamical minimum indicates that several orbitals, typically the valence molecular orbitals (HOMO-1, ...) lying close below the highest-occupied one (HOMO), are energetically high enough to contribute to the first stage of HHG, namely the tunneling ionization process (step (i)). During the continuum excursion (step (ii)) prior to recombination (step (iii)), they leave the molecular ion in a coherent superposition of the ground (X) and excited states (A, B, ...). All these ionization channels finally coherently contribute to the harmonic emission [20, 21] which encodes the ultrafast dynamics occurring in the molecular ion during the emission process, giving access, e.g., to the rearrangements taking place in the electronic shells within less than one laser cycle [22, 23].

Disentangling the contributions of the different ionization channels thus requires an advanced characterization of the harmonic emission, including the measurements, not only of the spectral intensities of the harmonic components [14, 15, 19, 21, 24, 26], but also of their relative phases. As explained in Sect. 11.2, this can be achieved with the help of the RABBIT technique. For the sake of illustration,

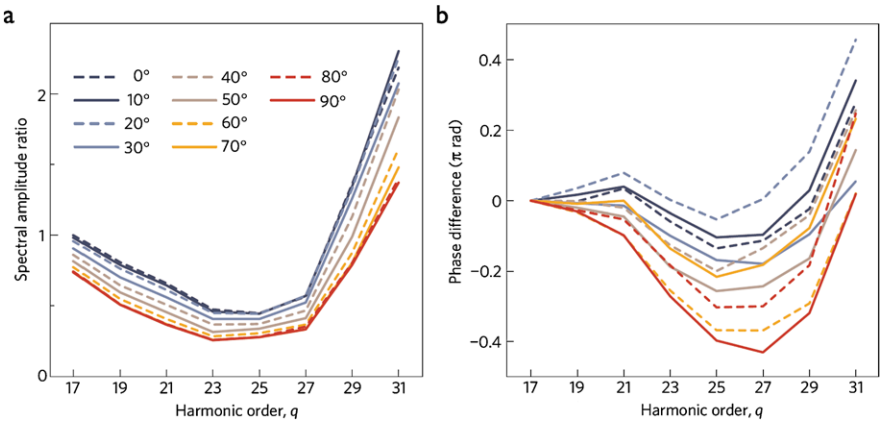

Fig. 11.1 Experimental recombination dipole for N_2 molecules. Amplitude (**a**) and phase (**b**) of the complex soft-X-ray field for N_2 at various alignment angles normalized by that for argon. For perpendicular alignment ($\theta = 90°$), the phase decreases by $\pi/2$ between harmonic H_{17} and H_{27}. This change gradually disappears when rotating the molecules towards parallel alignment ($\theta = 0°$). For all angles, the phase increases by $\pi/2$ from H_{27} on, which might be the beginning of a larger jump not completely contained in our spectral range. The phase difference is set to 0 at the lowest harmonic order H_{17}

we present the measurements of the angular dependence of the harmonic yields and phases, in the specific case of N_2 as generating medium, at a fixed intensity (1.2×10^{14} W/cm^2) in Fig. 11.1 [5].

In that system, the global phase difference between the contributions of the HOMO and of the HOMO-1 orbitals for harmonic 25 is close to $\pi/2$ [5]. Therefore, their contributions to the normalized molecular dipole are practically disentangled in the imaginary and real part respectively. A more detailed analysis of the complex dipole structure allows the exploitation of the measured data: (i) to simulate the temporal profiles of the attosecond emission, (ii) to reconstruct the involved orbitals by a tomographic procedure, and, merging the temporal and structural aspects, (iii) to image, at the instant of recombination, the dynamical "hole" formed by the coherent ionization channels [5].

Pursuing that type of investigation by varying the laser intensity I_L, one can evidence the changes in HHG when exploring frequencies below and above the cut-off. Again, in the case of N_2, this is achieved when varying I_L between 0.7×10^{14} W/cm^2 (cut-off at H_{21}) and 1.3×10^{14} W/cm^2 (cut-off at H_{29}). One can observe a fast variation of the harmonic phase as a function of the harmonic order, while the harmonic intensity presents a shallow I_L-independent minimum, as shown in Fig. 11.2 [6].

Two mechanisms were identified to explain this measured non-trivial phase evolution. First, the difference in the continuum dynamics of the two channels controls the harmonic phase in the cut-off region. Second, the remarkably fast—sub-cycle—nuclear dynamics occurring on the attosecond timescale in the A channel strongly affects its contribution to HHG. Typically, in N_2, the non-trivial HHG phase changes

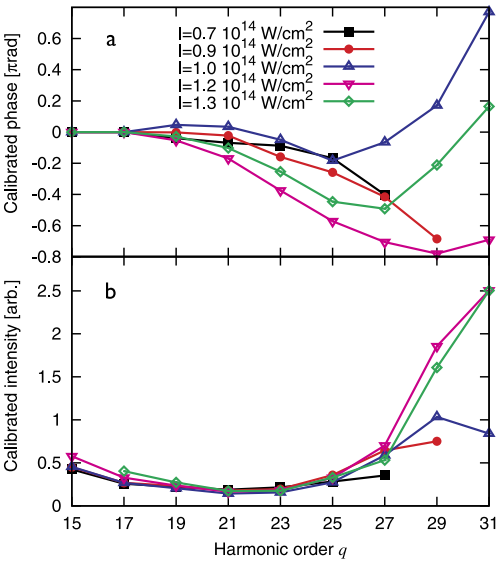

Fig. 11.2 Pump laser intensity-dependent harmonic phases (**a**) and intensities (**b**) measured for N_2 at $\theta = 90°$ and respectively calibrated with Ar quantities for different driving laser intensities indicated in units of 10^{14} W/cm^2. All phases are moved to 0 at H_{15}

over the spectral range are attributed to variations of the X- and A-channel relative amplitudes and phases, up to a situation where the A channel contribution is significantly reduced. Therefore, the relative magnitudes of the contributions of different orbitals (here principally the HOMO and HOMO-1) to HHG can be controlled through a fine tuning of the laser intensity.

11.3.2 Control in Time of Harmonic Emission

Generating attosecond pulse trains in aligned molecules does not only provide a signal that encodes information about the molecular structure and dynamics, but it also provides a mean to coherently control the attosecond time profile of the XUV emission. This has been demonstrated on the example of the attosecond high harmonic emission from aligned CO_2 molecules [7]. Again, much similarly to the previously discussed case of N_2, the laser intensity appears as a key parameter to control the different orbital contributions.

Figure 11.3 shows spectral intensities and emission times measured with the RABBIT method for CO_2 molecules, the internuclear axis of which has been aligned at varying angles θ with respect to the driving laser polarization direction. These data have been obtained with a driving laser pulse of 55 fs duration and an intensity of 0.95×10^{14} W/cm^2. The spectral intensities show a strong dependence on alignment angle around the harmonic orders 23 and 25: for the parallel alignment ($\theta = 0°$), their intensities are suppressed by about one order of magnitude as compared to perpendicular alignment ($\theta = 90°$). Correlated with this suppression, a "hump" on the emission time curves is observed, which appears on top of the usual linear increase with harmonic order, typical for the short trajectory contribution to

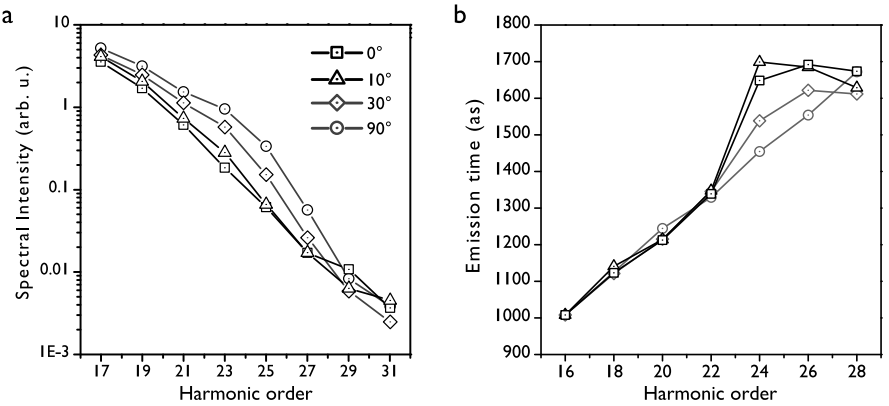

Fig. 11.3 Spectral Intensities (**a**) and emission times (**b**) for CO_2 aligned at $\theta = 0°$ (*squares*), 10° (*triangles*), 30° (*diamonds*) and 90° (*circles*). These data are taken from the series of measurements also used for Fig. 3 in [7]

HHG. The emission times are the derivative of the harmonic spectral phase with respect to frequency—namely the group delay, i.e. the hump corresponds to a rapid phase increase, or a phase jump. In these experiments, the value of this phase jump has been found to be (2.0 ± 0.6) rad in a series of 8 independent measurements for $\theta = 0°$. The angle-dependent intensity minimum correlated to a phase jump is a clear sign for destructive quantum interference taking place in HHG. While in [7], structural interference appearing around harmonic photon energies of 60 eV [24, 25] has been initially proposed as the main origin, it later turned out that dynamic interference of the two channels involving the HOMO and HOMO-2 of CO_2 [20] is the most likely explanation of the observations.

Indeed, whatever the physical process behind, the destructive interference can however be controlled by the choice of the molecule, the alignment, and possibly the driving laser intensity. This opens the possibility to control the temporal profile of the emitted attosecond pulses. Figure 11.4(a) and (b) shows reconstructions of the temporal intensity profiles of the attosecond pulses emitted by CO_2 molecules aligned at varying angles $\theta = 0°, 10°, 20°, \ldots, 90°$ for two different spectral ranges. The data used for these reconstructions is from the same series of RABBIT scans, of which Fig. 11.3 shows a selection. Including only harmonic orders below the phase jump in the attosecond pulse reconstruction leads to pulses whose shape and timing are independent of the molecular alignment. They also have the same duration of 320 as FWHM and timing as the attosecond pulses generated in the 'reference atom' krypton, which has the same ionization potential as CO_2. However, including only the harmonic orders undergoing the phase jump in the attosecond pulse reconstruction, the obtained intensity profile for $\theta = 0°$ is delayed by 150 as with respect to the krypton emission, and gradually evolves in agreement with the reference atom as the molecules are rotated towards perpendicular alignment ($\theta = 90°$) [7]. The delayed emission is due to the spreading of the phase jump over several harmonic orders, which leads to the corresponding emission times being shifted to larger values.

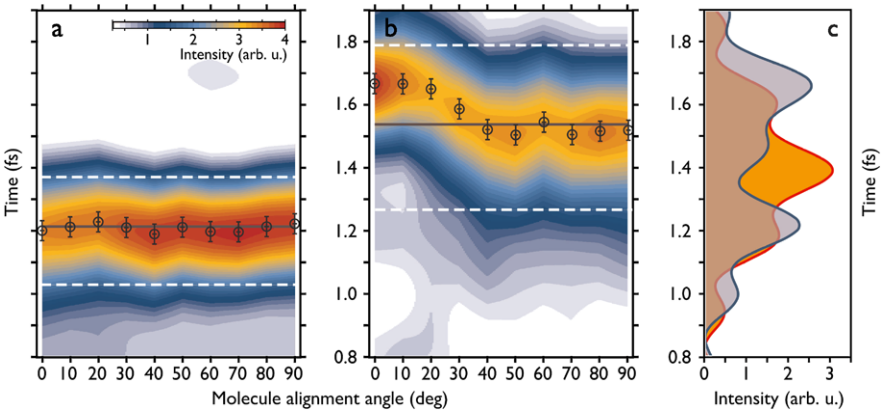

Fig. 11.4 Intensity of a typical attosecond pulse in the generated train, mapped as a function of the alignment angle θ and time t, with $t = 0$ at the maximum of the generating laser field. *Circles* give the peak position of the pulse in a series of RABBIT scans, and the error bars represent the standard deviation of the emission time of sideband SB_{16}, indicating the error in absolute timing of the attosecond pulses. *Black and dashed white lines* indicate the positions of peak and half–maximum, respectively, of the attosecond pulse generated in krypton under the same experimental conditions. (**a**) Using harmonics H_{17}–H_{23}, located below the phase jump, and (**b**), using harmonics H_{23}–H_{29}, undergoing the phase jump. (**c**) Using harmonics H_{17}–H_{29} and assuming constant spectral amplitudes for $\theta = 0°$ (*blue*) and $\theta = 90°$ (*orange*). (Figure adapted from [7])

Assuming that with spectral filters we are able to transform our measured spectral amplitudes into flat ones and including the whole spectral range (harmonics H_{17}–H_{29}) into the reconstruction, strongly distorted pulse time profiles are obtained, as shown in Fig. 11.4(c). For $\theta = 0°$ and thus for a strong phase jump, destructive interference between the parts of the spectrum before and after the phase jump causes a dip in the temporal intensity. This dip appears just at the temporal position where constructive interference of all spectral components builds up the pulse peak in the case of $\theta = 90°$, where there is no phase jump. Rotating the molecules can thus switch the pulse time profile from a single to a double peak structure.

What are the possible applications of this pulse shaping method? XUV pulse shaping can be achieved, of course, partly by amplitude shaping using filters or specifically designed mirrors. Including only certain harmonic orders in the APT reconstruction is already a 'virtual' amplitude shaping. The most interesting feature of aligned molecules as an APT source is the phase jump that can be switched on and off and placed at a chosen spectral position according to the molecule, its alignment, and possibly the driving laser intensity. The capability of adding a phase jump, close to π, at some spectral position is a central element in any pulse shaping scheme [27], which has until recently not been available in the XUV regime. Such a phase jump, placed at the transition energy, can serve to transiently enhance a resonant transition [28], which is one of the simplest coherent control schemes. Below- and above-resonance contributions to the excited state population then interfere constructively and result in so called coherent transients. The phase jump

in the XUV emission from aligned molecules can thus be used to drive a transient enhancement of the population of a spectrally large resonance in the XUV region.

11.4 Molecular Photoionization with Attosecond XUV Harmonic Pulses

As explained in the previous sections, the RABBIT method was developed (and successfully applied) to characterize ultrashort XUV pulse trains produced in HHG, through the retrieval of the harmonic phases $\Delta\phi_\Omega$ (see Eq. (11.1)). To achieve this goal, the implementation of the RABBIT technique assumes that the harmonics are detected in a reference gas with known or negligible atomic/molecular phases $\Delta\theta$.

However, the method was recently used in a non-conventional way, where a gas is ionized with characterized harmonics and the atomic/molecular phases $\Delta\theta$ are deduced from RABBIT measurements [8, 9, 29, 30]. This came with new issues concerning the interpretation of the experimental data: What information is encoded in $\Delta\theta$? To be more specific, what can be learned from these phases in terms of ionization dynamics? Up to date, two different—but not contradictory—answers were proposed. In [30], it was shown that, close to the ionization threshold with the constraint that $\Delta\theta$ varies smoothly with energy, it gives access to a characteristic time-delay τ_I (see Eq. (11.2)) that is reminiscent of the so-called "Wigner time-delay". The latter is defined as the energy derivative of the scattering phase shift of the photoelectron wave function [31]. In this section, we focus on a complementary interpretation, introduced in [9], which relates the *spectral derivative* of $\Delta\theta$ to the sideband formation delay [32].

11.4.1 RABBIT Phase and Time Delays

The two paths leading to a given sideband can be seen as two "quantum slits" through which the released electron wave-packet is coherently formed. The phase $\Delta\theta$ is nothing but the phase difference accumulated by the wave packet *during its formation* through each of the paths, irrelevant of the IR and XUV fields phases.

This translates into the time domain by assigning, to each path leading to a given sideband SB_{2q}, a "generalized group delay" defined as

$$\tau_\pm = \frac{1}{2q \pm 1}\frac{\partial\theta_\pm}{\partial\omega_L}, \tag{11.6}$$

where $\theta_\pm$ are the phases of the two-photon matrix elements associated to each path, as defined in Eq. 11.5 [32]. These delays then appear in the spectral variations of the SB_{2q} RABBIT phase as:

$$\frac{1}{2q}\frac{\partial\Delta\theta}{\partial\omega_L} = \frac{1}{2q}\left(\frac{\partial\theta_+}{\partial\omega_L} - \frac{\partial\theta_-}{\partial\omega_L}\right) \tag{11.7}$$

$$= \frac{2q+1}{2q}\tau_+ - \frac{2q-1}{2q}\tau_-. \tag{11.8}$$

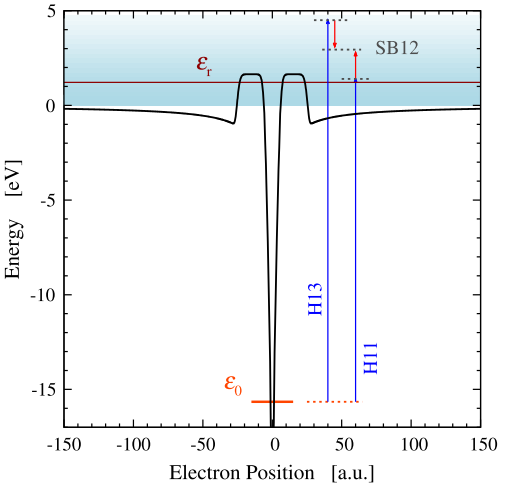

Fig. 11.5 Model system. The potential (*full black line*) is composed of a soft-coulomb binding term, adjusted for a ground state energy $\varepsilon_0 = -15.65$ eV, to which a symmetric barrier is added to create a shape resonance of width $\Gamma_r \approx 10$ meV at $\varepsilon_r = 1.22$ eV. Starting from the ground state, the 11th harmonic of a ~ 800 nm laser hits the vicinity of the resonance, while the 13th harmonic reaches a smooth region of the continuum. This model potential corresponds actually to a cut in the potential of the more elaborate molecular model used in Ref. [9]

For sufficiently large orders q, the latter can be approximated as

$$\frac{1}{2q}\frac{\partial \Delta\theta}{\partial \omega_L} \simeq \tau_+ - \tau_- \tag{11.9}$$

The RABBIT phase derivative thus provides the sideband group delay difference, through each of the interfering paths.

11.4.2 Physical Meaning of the Delays

The physical meaning of these delays was evidenced in [9], in numerical experiments where the delays derived from RABBIT simulations were compared to wavepacket "times-of-flights (TOF)", as suggested by Eq. (11.9). The simulations were performed on a model molecule accounting for the essential vibronic features of N_2, on which preliminary experimental results had been reported, in a situation where one of the paths leading to the sideband strongly differs from the other [8].

Here, we illustrate the method with similar simulations on a simple, one-dimensional (1D), model system (see Fig. 11.5). The model potential was designed to present a shape resonance with energy $\varepsilon_r = 1.22$ eV above threshold, i.e. at about 17 eV above the ground state ($\varepsilon_0 = -15.65$ eV). The energy difference corresponds to the energy of the 11th harmonic of a 800 nm Ti:Sapph laser ($\omega_L \approx 1.55$ eV). When simulating a RABBIT experiment, the path leading to SB_{12} through H_{11} is

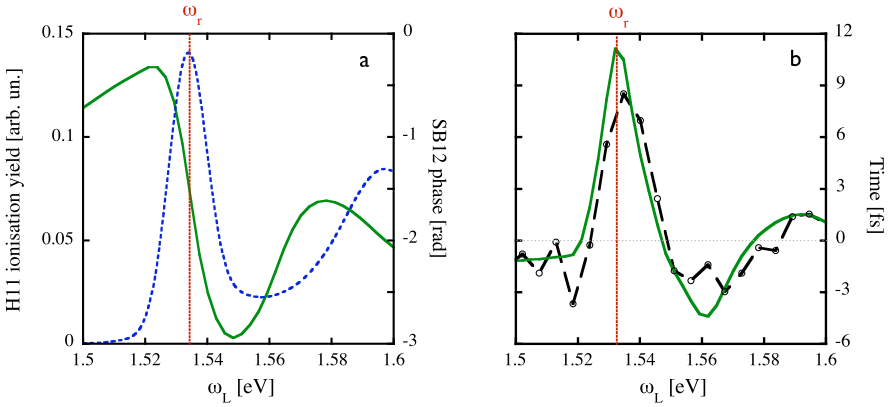

Fig. 11.6 (**a**) Probability to photoionize the system with H_{11} as a function of the fundamental frequency ω_L (*blue dashed curve*); SB_{12} RABBIT phase obtained by photoionizing the system with H_{11}, H_{13} and the fundamental (*green full curve*). (**b**) Group delay difference $\tau_+ - \tau_-$ retrieved through numerical differentiation of the RABBIT phase according to Eq. (11.9) (*green full curve*); Photoionization delay difference $\tilde{\tau}_+ - \tilde{\tau}_-$ obtained by TOF-like detection of the SB_{12} wave-packets (*empty circles* linked by *black dashed lines*). The frequency ω_r at which H_{11} hits the sharp resonance is indicated by a *vertical red dotted line*

therefore affected by the resonance, in contrast with the upper path involving H_{13} through a smooth continuum. Such simulations were realized by solving ab initio the corresponding time-dependent Schrödinger equation (TDSE) for the system. The laser frequencies were chosen to explore the vicinity of the resonance with field intensities kept low enough to make negligible the transitions involving more than two photons.

In a first stage, we computed the ionization probability with H_{11} only, when varying the *fundamental* frequency ω_L between 1.5 and 1.6 eV. This provides a clear picture of the structure of the system's spectrum in the vicinity of the resonance. The result is displayed on frame (a) of Fig. 11.6(dashed blue curve). The resonance we are interested in is responsible for the prominent peak localized at $\omega_r = (\varepsilon_r - \varepsilon_0)/11 \approx 1.53$ eV. Its width is governed by the spectral width of the H_{11} pulse, which exceeds the resonance's width Γ_r by about one order of magnitude. In addition, a broader resonance is revealed at higher energies, for $\omega_L \approx 1.6$ eV.

Then, we simulated the photoionization of the model system in the presence of the XUV harmonics 11 and 13, as well as of the fundamental IR. Electron spectra were obtained by a spectral Fourier analysis of the final wave-function, and RABBIT phases were retrieved from the SB_{12} oscillations observed when tuning the XUV-IR delay τ (see Sect. 11.2). The procedure was repeated for a set of frequencies in the range of interest. The results are presented in Fig. 11.6. The vertical dashed line indicates the resonant laser frequency ω_r, for which $\Omega_- = 11 \times \omega_L = 16.87$ eV. We see that the RABBIT phase (frame (a) of Fig. 11.6) undergoes a $-\pi$ jump when Ω_- crosses the resonance. This corresponds to the change of sign of the denominator in the term (thus by far dominant) associated to the resonant state $n = r$

in the corresponding two-photon transition matrix element shown in Eq. (11.3). Another negative, but less pronounced, jump takes place as H_{11} enters the vicinity of the second, broader, resonance. In addition, a third jump (now positive) takes place *between* the resonances, around $\omega_L \approx 1.56$ eV. The latter results from an almost zero in the two-photon transition probability, where the contributions from the two consecutive resonances compensate each other, leaving only the contribution from the smooth continuum. Note that the two *vibronic* resonances identified in [9] correspond to two vibrational states associated to the same electronic resonance, while here they correspond to two different electronic states of our simpler 1D model. By contrast, we have checked that a typical—resonance-free—RABBIT phase varies by less than few tenths of radians within this range of laser frequencies.

We now turn to the generalized group delay difference $\partial\Delta\theta/(12\partial\omega_L)$ as given by Eq. (11.9), obtained by numerical differentiation of the RABBIT phases. It is displayed as the green full curve in frame (b) of Fig. 11.6. Each jump observed in the phase translates into a delay difference of several femtoseconds, up to ≈ 10 fs at ω_r: On the time scale of photoionization, it is a dramatic change in duration, as compared e.g. to Wigner-like delays which typically do not exceed a few tens of attoseconds [30, 33].

Whether such a delay difference—derived from a set of RABBIT phases—has any physical reality, was checked with the help of another series of simulations, where the model system was photoionized by either H_{11} or H_{13}, in addition to the fundamental. This corresponds respectively to the lower and upper paths leading to SB_{12} in the previous RABBIT simulations. Here we have performed "numerical time-of-fligth (TOF)" evaluations by computing, for each path, the electron flux at a given distance from the core. The latter was chosen large enough to make sure that the electron wave-packet associated to SB_{12} reaches the virtual detector when the interaction with the XUV and IR fields is over. At each considered frequency, the flux temporal profile reflects the pulse shape (not shown). The time at which it is maximum is a good indicator of the SB_{12} wave-packet arrival time at the virtual detector (noted $\tilde{\tau}_-$ and $\tilde{\tau}_+$ for the lower and upper paths respectively). Note that, while the values of $\tilde{\tau}_+$ and $\tilde{\tau}_-$ obviously depend on the detector's position, the difference $\tilde{\tau}_+ - \tilde{\tau}_-$ does not, because the two wave-packets evolve with the same total energy, along the same potential.

We have reported the arrival time difference $\tilde{\tau}_+ - \tilde{\tau}_-$ as a function of ω_L in frame (b) of Fig. 11.6(empty circles connected by black dashed lines), and found an excellent agreement with the RABBIT derived group delay difference (green full curve, same plot).

Comparing these two sets of data demonstrates that the group delay differences derived from RABBIT data uncover the presence of a chronology in two-photon ATI transitions, which is not measurable otherwise with current TOF technologies. As both wave-packet components evolve identically once formed, this group delay difference can be ascribed to a difference of time spent prior to their release, i.e. during their formation. This can therefore be viewed as a time during which the system is "trapped" in the intermediate stage of the two-photon absorption, although the XUV and IR pulses act simultaneously, i.e. in an a priori non-sequential regime. An

interesting point, besides the possibility to measure such delays, is that the transition duration can be controlled by tuning the laser frequency around resonances.

11.5 Conclusions

In this chapter, we have presented recent experimental and theoretical results on the study of a new class of molecular processes that have been uncovered with the help of coherent XUV harmonic radiations. We have reported advances realized in two main domains of applications that have been explored so far: (i) Characterization and control of the harmonic emission, with applications to molecular structure issues; (ii) Use of harmonic radiation to evidence temporal aspects of the non-linear response of molecular systems. Thanks to the temporal structure of the harmonic pulse trains, it is now feasible to follow the temporal evolution of such systems, at the attosecond level. Here, the emphasis has been on the IR-XUV RABBIT technique which has revealed itself as an efficient tool to follow in time the changes in the electronic distribution within a molecule. So far, these studies have been conducted in simple molecules and, as such, they should be considered as proofs of principle. In any case, they open most interesting perspectives towards the study in real time of electronic processes in reactive systems.

References

1. V. Véniard, R. Taïeb, A. Maquet, Phys. Rev. Lett. **74**, 4161 (1995)
2. V. Véniard, R. Taïeb, A. Maquet, Phys. Rev. A **54**, 721 (1996)
3. H.G. Muller, Appl. Phys. B **74**, S17 (2002)
4. J. Itatani, J. Levesque, D. Zeidler, H. Niikura, H. Pépin, J.C. Kieffer, P.B. Corkum, D.M. Villeneuve, Nature **432**, 867 (2004)
5. S. Haessler, J. Caillat, W. Boutu, C. Giovanetti-Teixeira, T. Ruchon, T. Auguste, Z. Diveki, P. Breger, A. Maquet, B. Carré, R. Taïeb, P. Salières, Nat. Phys. **6**, 200 (2010)
6. Z. Diveki, A. Camper, S. Haessler, T. Auguste, T. Ruchon, B. Carré, P. Salières, R. Guichard, J. Caillat, A. Maquet, R. Taïeb, New J. Phys. **14**, 023062 (2012)
7. W. Boutu, S. Haessler, H. Merdji, P. Breger, G. Waters, M. Stankiewicz, L.J. Frasinski, R. Taïeb, J. Caillat, A. Maquet, P. Monchicourt, B. Carré, P. Salières, Nat. Phys. **4**, 545 (2008)
8. S. Haessler, B. Fabre, J. Higuet, J. Caillat, T. Ruchon, P. Breger, B. Carré, E. Constant, A. Maquet, E. Mével, P. Salières, R. Taïeb, Y. Mairesse, Phys. Rev. A **80**, 011404 (2009)
9. J. Caillat, A. Maquet, S. Haessler, B. Fabre, T. Ruchon, P. Salières, Y. Mairesse, R. Taïeb, Phys. Rev. Lett. **106**, 093002 (2011)
10. P.M. Paul, E.S. Toma, P. Breger, G. Mullot, F. Augé, Ph. Balcou, H.G. Muller, P. Agostini, Science **292**, 1689 (2001)
11. Y. Mairesse, A. de Bohan, L.J. Frasinski, H. Merdji, L.C. Dinu, P. Monchicourt, P. Breger, M. Kovačev, R. Taïeb, B. Carré, H.G. Muller, P. Agostini, P. Salières, Science **302**, 1540 (2003)
12. M. Lein, N. Hay, R. Velotta, J.P. Marangos, P.L. Knight, Phys. Rev. Lett. **88**, 183903 (2002)
13. M. Lein, N. Hay, R. Velotta, J.P. Marangos, P.L. Knight, Phys. Rev. A **66**, 023805 (2002)
14. C. Vozzi, F. Calegari, E. Benedetti, J.-P. Caumes, G. Sansone, S. Stagira, M. Nisoli, R. Torres, E. Heesel, N. Kajumba, J.P. Marangos, C. Altucci, R. Velotta, Phys. Rev. Lett. **95**, 153902 (2005)

15. T. Kanai, S. Minemoto, H. Sakai, Nature **435**, 470 (2005)
16. E. van der Zwan, M. Lein, Phys. Rev. A **82**, 033405 (2010)
17. J. Higuet, H. Ruf, N. Thiré, R. Cireasa, E. Constant, E. Cormier, D. Descamps, E. Mével, S. Petit, B. Pons, Y. Mairesse, B. Fabre, Phys. Rev. A **83**, 053401 (2011)
18. H.J. Wörner, H. Niikura, J.B. Bertrand, P.B. Corkum, D.M. Villeneuve, Phys. Rev. Lett. **102**, 103901 (2009)
19. H.J. Wörner, J.B. Bertrand, P. Hockett, P.B. Corkum, D.M. Villeneuve, Phys. Rev. Lett. **104**, 233904 (2010)
20. O. Smirnova, Y. Mairesse, S. Patchkovskii, N. Dudovich, D. Villeneuve, P. Corkum, M.Y. Ivanov, Nature **460**, 972 (2009)
21. B.K. McFarland, J.P. Farrell, P.H. Bucksbaum, M. Gühr, Science **322**, 1232 (2008)
22. O. Smirnova, S. Patchkovskii, Y. Mairesse, N. Dudovich, M.Y. Ivanov, Proc. Natl. Acad. Sci. USA **106**, 16556 (2009)
23. Y. Mairesse, J. Higuet, N. Dudovich, D. Shafir, B. Fabre, E. Mével, E. Constant, S. Patchkovskii, Z. Walters, M.Yu. Ivanov, O. Smirnova, Phys. Rev. Lett. **104**, 213601 (2010)
24. R. Torres, T. Siegel, L. Brugnera, I. Procino, J.G. Underwood, C. Altucci, R. Velotta, E. Springate, C. Froud, I.C.E. Turcu, S. Patchkovskii, M.Yu. Ivanov, O. Smirnova, J.P. Marangos, Phys. Rev. A **81**, 051802 (2010)
25. C. Vozzi, M. Negro, F. Calegari, G. Sansone, M. Nisoli, S. De Silvestri, S. Stagira, Nat. Phys. **7**, 823 (2011)
26. A.-T. Le, R.R. Lucchese, C.D. Lin, J. Phys. B **42**, 21 (2009)
27. A. Monmayrant, S. Weber, B. Chatel, J. Phys. B **43**, 103001 (2010)
28. N. Dudovich, D. Oron, Y. Silberberg, Phys. Rev. Lett. **88**, 123004 (2002)
29. M. Swoboda, T. Fordell, K. Klünder, J.M. Dahlström, M. Miranda, C. Buth, K.J. Schafer, J. Mauritsson, A. L'Huillier, M. Gisselbrecht, Phys. Rev. Lett. **104**, 103003 (2010)
30. K. Klünder, J.M. Dahlström, M. Gisselbrecht, T. Fordell, M. Swoboda, D. Guénot, P. Johnsson, J. Caillat, J. Mauritsson, A. Maquet, R. Taïeb, A. L'Huillier, Phys. Rev. Lett. **106**, 143002 (2011)
31. E.P. Wigner, Phys. Rev. **98**, 145 (1955)
32. M. Vacher et al. in preparation (2013)
33. M. Schultze, M. Fieß, N. Karpowicz, J. Gagnon, M. Korbman, M. Hofstetter, S. Neppl, A.L. Cavalieri, Y. Komninos, Th. Mercouris, C.A. Nicolaides, R. Pazourek, S. Nagele, J. Feist, J. Burgdörfer, A.M. Azzeer, R. Ernstorfer, R. Kienberger, U. Kleineberg, E. Goulielmakis, F. Krausz, V.S. Yakovlev, Science **328**, 1658 (2010)